Petroleum Science 20 (2023) 2113–2126

Contents lists available at ScienceDirect

Petroleum Science

journal homepage: www.keaipublishing.com/en/journals/petroleum-science

Original Paper

A joint absorbing boundary for the multiple-relaxation-time lattice Boltzmann method in seismic acoustic wavefield modeling

Chun-Tao Jiang [a], Hui Zhou [a, *], Mu-Ming Xia [b], Han-Ming Chen [a], Jin-Xuan Tang [c]

[a] State Key Laboratory of Petroleum Resources and Prospecting, CNPC Key Lab of Geophysical Exploration, China University of Petroleum, Beijing, 102249, China
[b] CAS Engineering Laboratory for Deep Resources Equipment and Technology, Institute of Geology and Geophysics, and Innovation Academy for Earth Science, Chinese Academy of Sciences, Beijing, 100029, China
[c] Research Institute of Petroleum Exploration & Development, PetroChina, Beijing, 100083, China

ARTICLE INFO

Article history:
Received 10 May 2022
Received in revised form
28 December 2022
Accepted 19 February 2023
Available online 2 March 2023

Edited by Jie Hao

Keywords:
Multiple-relaxation-time
Lattice Boltzmann method
Seismic acoustic wavefield simulation
Truncated Boundary reflection
Joint absorbing boundary

ABSTRACT

Conventional seismic wave forward simulation generally uses mathematical means to solve the macroscopic wave equation, and then obtains the corresponding seismic wavefield. Usually, when the subsurface structure is finely constructed and the continuity of media is poor, this strategy is difficult to meet the requirements of accurate wavefield calculation. This paper uses the multiple-relaxation-time lattice Boltzmann method (MRT-LBM) to conduct the seismic acoustic wavefield simulation and verify its computational accuracy. To cope with the problem of severe reflections at the truncated boundaries, we analogize the viscous absorbing boundary and perfectly matched layer (PML) absorbing boundary based on the single-relaxation-time lattice Boltzmann (SRT-LB) equation to the MRT-LB equation, and further, propose a joint absorbing boundary through comparative analysis. We give the specific forms of the modified MRT-LB equation loaded with the joint absorbing boundary in the two-dimensional (2D) and three-dimensional (3D) cases, respectively. Then, we verify the effects of this absorbing boundary scheme on a 2D homogeneous model, 2D modified British Petroleum (BP) gas-cloud model, and 3D homogeneous model, respectively. The results reveal that by comparing with the viscous absorbing boundary and PML absorbing boundary, the joint absorbing boundary has the best absorption performance, although it is a little bit complicated. Therefore, this joint absorbing boundary better solves the problem of truncated boundary reflections of MRT-LBM in simulating seismic acoustic wavefields, which is pivotal to its wide application in the field of exploration seismology.

1. Introduction

The numerical simulation of seismic wavefields is a highly important fundamental problem in seismology (Ba et al., 2008; Wang et al., 2019; Wang et al., 2020). In general, it is recognized that the motion of seismic waves in the subsurface medium can be well described by the macroscopic wave equation and its corresponding variants. The wave equation is based on continuum mechanics and can be mathematically solved by certain numerical discretization schemes, such as the finite-difference method (FDM) (e.g., Zang et al., 2021), pseudo-spectral method (PSM) (e.g., Kosloff and Baysal, 1982; Klin et al., 2010), and finite element method (FEM) (e.g., Marfurt, 1984; Sotelo et al., 2021), to acquire the relevant seismic wavefields. In particular, FDM is the most widely accepted one in practical simulation and production, mainly attributed to its simplicity, high computational efficiency, and acceptable accuracy. However, for the macroscopic wave equation, when the structure of the media is complex or there are strong physical discontinuities, for example, faults or solid-fluid multiphase interfaces, the calculation results of the traditional wavefield simulation schemes are sometimes difficult to meet the needs of accurate wavefield calculations (Dhuri et al., 2017; Xia et al., 2022; Jiang et al., 2022).

The wave equation considers the wave problem in seismology from a macroscopic scale, it is also possible to seek a physical model for wavefield simulation from a mesoscopic perspective. The lattice Boltzmann method (LBM) is an alternative numerical simulation

* Corresponding author.
E-mail address: huizhou@cup.edu.cn (H. Zhou).

https://doi.org/10.1016/j.petsci.2023.02.019

method for solving the Navier-Stokes equation based on the Boltzmann equation, with contemporary statistical physics as its theoretical basis (He and Luo, 1997; Lallemand and Luo, 2000; Zadehgol, 2022). It attempts to achieve the simulation of complex physical phenomena at the macroscopic level by tracking the interactions of discrete particles on the mesoscopic scale. LBM originated from the lattice gas automata (LGA) (Frisch et al., 1986), and was first proposed by McNamara and Zanetti (1988). The LBM algorithm is easy to understand and implement and has good stability. Because LBM is a mesoscopic method, there is no need to make continuity assumptions of the wave equations. In addition, due to its flexible boundary processing and completely discrete characteristics, it is very suitable for dealing with irregular boundaries and wavefield simulations of multiphase porous media (Dhuri et al., 2017; Xia et al., 2022). Through the remarkable contributions of many predecessors, LBM has developed rapidly in the fields of computational fluid dynamics, thermodynamics, and electromagnetics (e.g., Chen and Doolen, 1998; He and Doolen, 2002; Krüger et al., 2017; Hauser and Verhey, 2019; Wang et al., 2019). Nowadays, the most widely used and accepted one is the single-relaxation-time LBM (SRT-LBM) based on the Bhatnagar-Gross-Krook (BGK) collision operator (Qian et al., 1992), which is attributed to its high computational efficiency. However, another LBM method, called multiple-relaxation-time LBM (MRT-LBM) (e.g., Xu et al., 2012; Aslan et al., 2014; Wang, 2020) accompanied by multiple relaxation parameters, is also increasingly drawing researchers' interest, due to its higher computational accuracy, and better stability, etc. d'Humières (1992) first proposed MRT-LBM in rarefied gas dynamics, and then d'Humières (2002) provided a concise exposition of the MRT-LB equation and demonstrated its superior numerical stability over the popular lattice-BGK equation. Yu and Fan (2010) developed an MRT interaction-potential-based lattice Boltzmann model for two-phase flow, which significantly enhanced the numerical stability at low viscosities. Then, Chai and Zhao (2012) performed a detailed Chapman-Enskog analysis where the force term effect was also included. And recently, Chai and Shi (2020) presented a unified framework of MRT-LBM for the Navier-Stokes and nonlinear convection equations and conducted some detailed analysis.

In recent years, LBM has been gradually introduced into seismology as an alternative new simulation scheme for wave propagation. Zhang et al. (2009) proposed a lattice Boltzmann model for a two-dimensional (2D) wave equation by using the higher-order moment method. O'Brien et al. (2012) successfully applied LBM to model the elastic wave propagation and performed a similar von Neumann stability analysis. In particular, Viggen (2014) covered the lattice Boltzmann acoustics systematically and comprehensively. After that, Xia et al. (2017) employed LBM to simulate wave propagation in viscous media and revealed the relationship between the relaxation time in LBM and the quality factor in the Kelvin-Voigt-based wave equation. Not long after, Dhuri et al. (2017) analyzed a linear lattice Boltzmann formulation for the simulation of linear acoustic wave propagation in heterogeneous media, and studied the numerical anisotropy of the dispersion relation on various 2D lattices. Escande et al. (2020) proposed the von Neumann stability analysis along with a Chapman-Enskog analysis for SRT-LBM for wave propagation in isotropic linear elastic solids and successfully computed surface waves for the first time by LBM for elastic solids.

For wave problems in seismology, an inescapable aspect is the treatment of truncated boundary reflections (Tang et al., 2021). Generally, the best absorbing boundary for the macroscopic wave equation is recognized as the perfectly matched layer (PML) scheme, which has been developed and enhanced by many scholars (e.g., Chen et al., 2014; Wang et al., 2019), since it was proposed by Berenger (1994). Similarly, when adopting LBM to analyze wave problems, a good absorbing boundary scheme will greatly impact the calculation results. Some researchers have studied the absorbing boundary issue of LBM in different fields. Most of them are aimed at the SRT-LB equation, and the primary developments are briefly summarized below.

Kam et al. (2007) introduced a sponge layer formulation by adding an attenuation term to the lattice Boltzmann equation and achieved a certain absorption effect. Tekitek et al. (2009) showed that the reflection of sound waves could be simply reduced by changing the advection step of the lattice Boltzmann algorithm on the nodes close to the interface. In the field of computational fluid dynamics, Vergnault et al. (2012) developed a sponge-layer absorbing boundary based on the relaxation time, when using LBM to solve the time evolution of nonlinear disturbances around an arbitrary base flow. This scheme is simple and low-cost in the calculation, but it needs more absorption layers to achieve a better absorption effect. Subsequently, Vergnault et al. (2013) adopted this sponge-layer absorbing boundary to settle the problem of noise source identification. After this, the sponge-layer was often used to handle the external nonreflecting boundaries for compressible flows (e.g., Zhuo and Sagaut, 2017; Feng et al., 2019). In particular, Najafi-Yazdi and Mongeau (2012) derived a non-reflecting boundary condition based on PML in the field of computational aeroacoustics. This scheme is theoretically capable of realizing exponential attenuation of boundary reflections, but the simulation is prone to instability if the attenuation parameters are not properly chosen. More recently, in the field of seismology, Jiang et al. (2020) introduced the viscous absorbing boundary during the numerical simulation of the LBM wavefield, and by changing the attenuation coefficient and function type, a better-truncated boundary reflection suppression performance was achieved. In addition to this, there are some other studies of absorbing boundaries for SRT-LBM, such as characteristic boundary conditions (e.g., Schlaffer, 2013; Heubes et al., 2014). The collision process of MRT-LBM is more complicated, and thus its absorbing boundary is less studied. However, given the higher accuracy, better stability, and more flexible adjustment of relaxation parameters in wavefield simulations, the wide application of MRT-LBM in acoustic wave problems is a general trend. As a result, it is imperative to choose a good absorbing boundary scheme for wavefield modeling using MRT-LBM. In this article, we extend the viscous absorbing boundary (VAB) and the PML absorbing boundary to the MRT-LB equation and further propose a joint absorbing boundary (JAB) by combining the two strategies to attenuate more effectively the boundary reflections during MRT-LBM wavefield simulations.

The remainder of this paper is organized as follows. First, we introduce the basic theory of MRT-LBM-based wavefield simulations, and derive specific expressions for the VAB, PML, and JAB in the framework of MRT-LBM; then, we verify the accuracy of the MRT-LBM-simulated wavefield, and further compare the performances of the three absorption boundary schemes by numerical examples; after this, we conduct some brief discussions and finally draw some conclusions.

2. Theory

2.1. Multiple-relaxation-time lattice Boltzmann model

The continuous and force-free Boltzmann equation (Krüger et al., 2017) reads

$$\frac{\partial f(\boldsymbol{x},\boldsymbol{c},t)}{\partial t}+c_\alpha\frac{\partial f(\boldsymbol{x},\boldsymbol{c},t)}{\partial x_\alpha}=\Omega(f), \tag{1}$$

where $f(\boldsymbol{x},\boldsymbol{c},t)$ is a mesoscopic quantity named the particle

distribution function describing the density of particles with particle velocity $\boldsymbol{c}$ at the position $\boldsymbol{x} = [x, z]$ for a 2D case or $\boldsymbol{x} = [x, y, z]$ for a 3D case and at time t, $\Omega(f)$ is the collision operator. The velocity discretization and the spatial and temporal discretization of Equation (1) are carried out in sequence, and the multiple-relaxation-time collision scheme is adopted, therefore the so-called multiple-relaxation-time lattice Boltzmann equation (Krüger et al., 2017) can be written as

$$\boldsymbol{f}(\boldsymbol{x} + \boldsymbol{c}_l \Delta t, t + \Delta t) - \boldsymbol{f}(\boldsymbol{x}, t) = -\Delta t \boldsymbol{M}^{-1} \boldsymbol{S}[\boldsymbol{m}(\boldsymbol{x}, t) - \boldsymbol{m}^{\mathrm{eq}}(\boldsymbol{x}, t)], \tag{2}$$

where Δt stands for temporal sampling interval, $\boldsymbol{S}$ is a diagonal matrix, $\boldsymbol{M}$ is a transformation matrix connecting the particle distribution function $\boldsymbol{f}(\boldsymbol{x}, t)$ and equilibrium distribution function $\boldsymbol{f}^{\mathrm{eq}}(\boldsymbol{x}, t)$ in velocity space, and the velocity moment vector $\boldsymbol{m}(\boldsymbol{x}, t)$ and equilibrium moment vector $\boldsymbol{m}^{\mathrm{eq}}(\boldsymbol{x}, t)$ in moment space via

$$\begin{cases} \boldsymbol{m} = \boldsymbol{M}\boldsymbol{f}, \\ \boldsymbol{m}^{\mathrm{eq}} = \boldsymbol{M}\boldsymbol{f}^{\mathrm{eq}}. \end{cases} \tag{3}$$

Since LBM differs from traditional macroscopic numerical methods, which discretizes velocity, it is necessary to introduce the concept of discrete velocity models. Conventionally, the discrete velocity sets are denoted by DdQq (Qian et al., 1992), where d is the number of spatial dimensions and q is the number of discrete velocities. The most commonly used discrete velocity sets include D1Q3, D2Q9, D3Q15, D3Q19, and D3Q27. Here, only D2Q9 and D3Q15 are introduced in detail. These two schemes are displayed in Fig. 1, whose discrete velocity sets respectively are

$$\begin{cases} \boldsymbol{c}_0 = (0, 0), \\ \boldsymbol{c}_{1-4} = (\pm 1, 0), (0, \pm 1), \\ \boldsymbol{c}_{5-8} = (\pm 1, \pm 1), \end{cases} \tag{4}$$

and

$$\begin{cases} \boldsymbol{c}_0 = (0, 0, 0), \\ \boldsymbol{c}_{1-6} = (\pm 1, 0, 0), (0, \pm 1, 0), (0, 0, \pm 1), \\ \boldsymbol{c}_{7-14} = (\pm 1, \pm 1, \pm 1). \end{cases} \tag{5}$$

The corresponding weighting factors are expressed respectively as

$$\begin{cases} w_0 = 4/9, \\ w_{1-4} = 1/9, \\ w_{5-8} = 1/36, \end{cases} \tag{6}$$

and

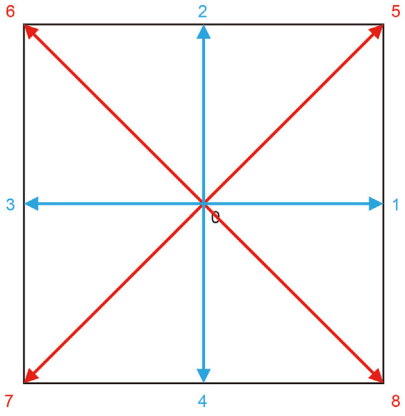

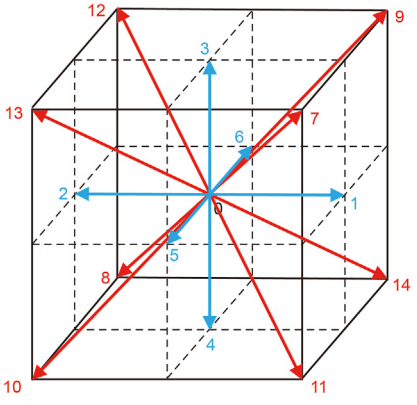

Fig. 1. The schematic diagram of (a) D2Q9 and (b) D3Q15 discrete velocity models for LBM, with the same color arrows in each subplot having the identical weighting factor.

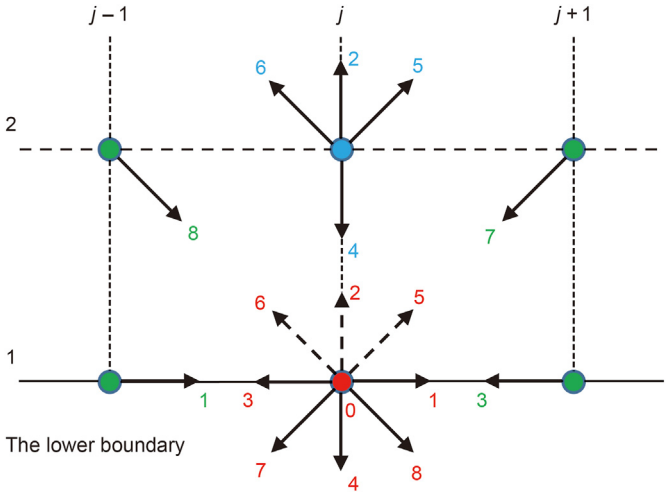

Fig. 2. The processing of unknown particle distribution functions (i.e., $f_{2,5,6}(1, j)$) for the lower boundary.

$$\begin{cases} w_0 = 2/9, \\ w_{1-6} = 1/9, \\ w_{7-14} = 1/72. \end{cases} \tag{7}$$

Interestingly, the speeds of sound for the D2Q9 and D3Q15 schemes are both $c_s = 1/\sqrt{3}$.

Another quantity in LBM is the equilibrium distribution function $\boldsymbol{f}^{\mathrm{eq}}(\boldsymbol{x}, t)$, its general form is defined as (Xia et al., 2017)

$$f_l^{\mathrm{eq}} = \rho w_l \left[1 + \frac{\boldsymbol{c}_l \cdot \boldsymbol{u}}{c_s^2} + \frac{(\boldsymbol{c}_l \cdot \boldsymbol{u})^2}{2c_s^4} - \frac{\boldsymbol{u}^2}{2c_s^2} \right], \tag{8}$$

where the dot stands for the inner product of two vectors, $l = 0, 1, \ldots, 8$ for D2Q9 and $l = 0, 1, \ldots, 14$ for the D3Q15 scheme, ρ and $\boldsymbol{u}$ are the macroscopic quantity density and vibration velocity vector, respectively. Generally, these two macroscopic quantities can be calculated through weighted sums known as moments of f_l.

$$\begin{cases} \rho = \sum_l f_l, \\ \boldsymbol{u} = \frac{1}{\rho} \sum_l f_l \boldsymbol{c}_l. \end{cases} \tag{9}$$

Then return to Equation (2), a straightforward and critical issue is how to deal with it. Indeed, the core steps include collision and

streaming processes. The first part is the collision

$$\boldsymbol{f}^{*}(\boldsymbol{x},t)=\boldsymbol{f}(\boldsymbol{x},t)-\Delta t\boldsymbol{M}^{-1}\boldsymbol{S}[\boldsymbol{m}(\boldsymbol{x},t)-\boldsymbol{m}^{\mathrm{eq}}(\boldsymbol{x},t)], \tag{10}$$

where $\boldsymbol{f}^{*}(\boldsymbol{x},t)$ represents the distribution function after the collision. Keep in mind that this step is performed in the moment space and is simply an algebraic local operation. The other part is streaming

$$\boldsymbol{f}(\boldsymbol{x}+\boldsymbol{c}_l\Delta t,t+\Delta t)=\boldsymbol{f}^{*}(\boldsymbol{x},t). \tag{11}$$

In contrast, this step is implemented in the velocity space. Usually, the trouble that is often encountered during the streaming step is that certain values of $f_l(\boldsymbol{x},t)$ for the nodes on the boundary are unknown. As a result, some boundary condition processing must be carried out in advance (e.g., Guo et al., 2002; Latt et al., 2008). In the following part, the distribution functions of node $(1,j)$ illustrated as a red spot in Fig. 2 at the lower boundary are considered as an example. Obviously, the values of $f_{2,5,6}(1,j)$ need to be confirmed, and an extrapolation scheme is introduced here for boundary processing

$$f_{2,5,6}(1,j)=f_{2,5,6}(2,j). \tag{12}$$

Of course, other boundary processing schemes (e.g., Mohammed and Reis, 2021) are also valid and optional, but are not described here.

Given that both MRT-LBM and the wave equation usually solved by FDM can be used to describe wave phenomena, it is interesting to compare the two in seismic wavefield propagation. The comparisons between MRT-LBM and FDM in terms of core algorithm, numerical discrete method and source loading are as follows.

(1) Core algorithm. MRT-LBM is a mesoscopic scale numerical algorithm that solves the Navier-Stokes equation. Its key steps are the collision process and the streaming process. FDM is a macro-scale numerical algorithm that can solve the conventional wave equation. The key step of FDM is to replace the time or space partial derivative of the wave equation with the difference, and iteratively obtain the pressure term and the vibration velocity term.
(2) Numerical discrete method. In addition to discretizing space and time, MRT-LBM also discretizes velocity. FDM, however, only discretizes space and time.
(3) Source loading. The source of MRT-LBM is generally loaded on the mesoscopic particle distribution function, while that of FDM is usually loaded on the macroscopic pressure or vibration velocity. In addition, the settings of initial conditions and boundary conditions are also different.

2.2. Viscous absorbing boundary

When using a certain numerical method to simulate the seismic wavefield, the suppression of the truncated boundary reflection is an inevitable problem. Vergnault et al. (2012) proposed an idea for SRT-LBM to achieve boundary attenuation through varying the relaxation time τ, which is primarily based on the close correlation between τ and the shear viscosity υ (Viggen, 2014)

$$\upsilon=c_s^2\left(\tau-\frac{1}{2}\right). \tag{13}$$

This idea is simple and extensible. Nevertheless, how to smoothly vary τ of the absorbing layer is a subject worth exploring. Naturally, it is straightforward to transfer this idea to MRT-LBM. Regarding D2Q9-based MRT-LBM, its diagonal matrix $\boldsymbol{S}$ in Equation (10) contains 9 relaxation parameters

$$\boldsymbol{S}=diag(s_1,s_2,s_3,s_4,s_5,s_6,s_7,s_8,s_9), \tag{14}$$

among them, s_2 and s_8 (or s_9) are related to bulk viscosity υ_B and shear viscosity υ, respectively

$$\begin{cases}\upsilon=c_s^2\left(\dfrac{1}{s_8}-\dfrac{1}{2}\right),\\ \upsilon_B=c_s^2\left(\dfrac{1}{s_2}-\dfrac{1}{2}\right)-\dfrac{1}{3}\upsilon.\end{cases} \tag{15}$$

In this way, it gives a theoretical basis for the viscous absorbing boundary. Basically, the three relaxation parameters do not change in the inner region (i.e., $s_l^{*}(x)=s_l$), while in the right absorbing region they can be expressed as

$$s_l^{*}(x)=\frac{1}{1/s_l+g(x)},\quad l=2,8,9, \tag{16}$$

where s_l is the relaxation parameter of the inner region, and $g(x)$ is a monotonically increasing function to be determined. The viscous absorbing boundary algorithm is uncomplicated. Unfortunately, the absorption effect is sensitive to $g(x)$ and not quite significant.

2.3. PML absorbing boundary

On the other hand, Najafi-Yazdi and Mongeau (2012) derived a PML-based absorbing boundary for the SRT-LB equation to suppress the truncated boundary reflection and achieved good effects. is convenient to apply this idea to the MRT-LBM-based continuous Boltzmann equation. Similarly, only the D2Q9 velocity model is considered here, therefore the discrete-velocity Boltzmann equation is simplified to

$$\frac{\partial\boldsymbol{f}}{\partial t}+\boldsymbol{P}\frac{\partial\boldsymbol{f}}{\partial x}+\boldsymbol{Q}\frac{\partial\boldsymbol{f}}{\partial z}=-\Delta t\boldsymbol{M}^{-1}\boldsymbol{S}[\boldsymbol{m}-\boldsymbol{m}^{\mathrm{eq}}], \tag{17}$$

where $\boldsymbol{P}=diag(c_{xl}),\boldsymbol{Q}=diag(c_{zl}),l=1,2,\cdots 9$. To load the PML absorbing boundary to the above equation, $\boldsymbol{f}$ must be decomposed as follows

$$\boldsymbol{f}=\boldsymbol{f}^{\mathrm{neq}}+\boldsymbol{f}^{\mathrm{eq}}=\boldsymbol{f}^{\mathrm{neq}}+\boldsymbol{h}+\boldsymbol{l}, \tag{18}$$

where $\boldsymbol{f}^{\mathrm{neq}}$ is the non-equilibrium distribution function, $\boldsymbol{h}$ and $\boldsymbol{l}$ are the perturbation component and mean component of $\boldsymbol{f}^{\mathrm{eq}}$, respectively. Further, decompose $\boldsymbol{h}$ into two terms $\boldsymbol{h}_1$ and $\boldsymbol{h}_2$, so that an attenuation term can be conveniently introduced

$$\begin{cases}\dfrac{\partial\boldsymbol{h}_1}{\partial t}+\alpha\boldsymbol{h}_1+\boldsymbol{P}\dfrac{\partial\boldsymbol{h}}{\partial x}=0,\\ \dfrac{\partial\boldsymbol{h}_2}{\partial t}+\alpha\boldsymbol{h}_2+\boldsymbol{Q}\dfrac{\partial\boldsymbol{h}}{\partial z}=0,\end{cases} \tag{19}$$

where α is the absorption attenuation factor. It is easy to prove that the above equation can achieve PML exponential attenuation of boundary reflections. Next, perform Fourier transformation on Equation (19) and do some simple algebraic operations, we have

$$i\omega\boldsymbol{H}-\frac{\omega}{i\alpha-\omega}\boldsymbol{P}\frac{\partial\boldsymbol{H}}{\partial x}-\frac{\omega}{i\alpha-\omega}\boldsymbol{Q}\frac{\partial\boldsymbol{H}}{\partial z}=0, \tag{20}$$

where i is the imaginary unit, and ω is the angular frequency. Then,

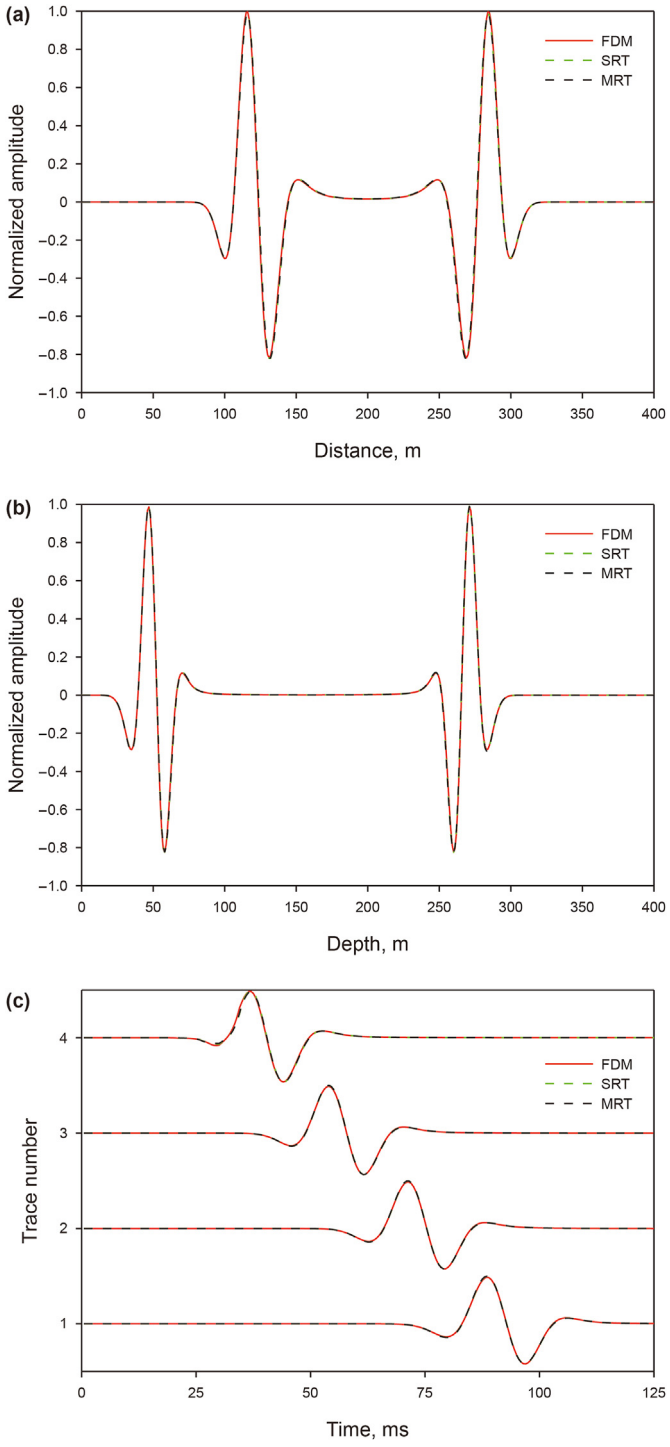

Fig. 3. Wave profiles at (a) $z = 250$ m and $t = 125$ ms and (b) $x = 150$ m and $t = 125$ ms, and (c) vibration records at (160 m, 120 m), (160 m, 140 m), (160 m, 160 m), and (160 m, 180 m) calculated by SRT-LBM (green dashed line), MRT-LBM (black dashed line) and FDM (red solid line), respectively.

through further derivations, the above equation can be rewritten as

Table 1
The quantitative differences of SRT-LBM and MRT-LBM relative to FDM calculated by Equation (25).

η_{SRT}	0.0562%	0.0604%	0.0875%	0.222%
η_{MRT}	0.0557%	0.0398%	0.0394%	0.183%

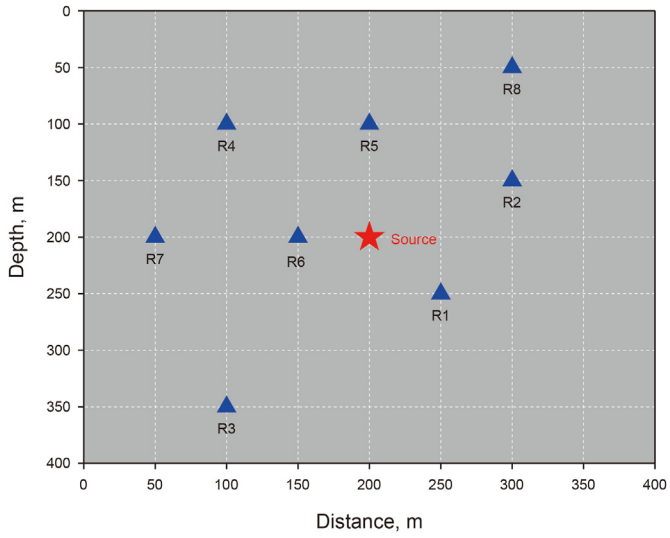

Fig. 4. The size of the homogeneous model and the setup of the observation positions, where the red star represents the source and the blue triangles represent eight receivers.

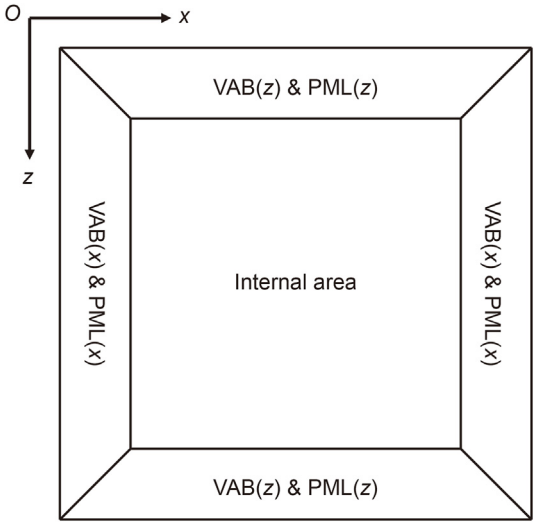

Fig. 5. Trapezoidal absorption layers designed for all three absorbing schemes. The absorption at the left and right absorbing regions is only related to x, and that at the upper and lower regions is just relevant to z.

$$i\omega \boldsymbol{H} + \boldsymbol{P}\frac{\partial \boldsymbol{H}}{\partial x} + \boldsymbol{Q}\frac{\partial \boldsymbol{H}}{\partial z} = \frac{i\alpha}{i\alpha - \omega}\left(\boldsymbol{P}\frac{\partial \boldsymbol{H}}{\partial x} + \boldsymbol{Q}\frac{\partial \boldsymbol{H}}{\partial z}\right) = -2\alpha \boldsymbol{H} - \frac{\alpha^2}{i\omega}\boldsymbol{H} - \frac{\alpha}{i\omega}\left(\boldsymbol{P}\frac{\partial \boldsymbol{H}}{\partial x} + \boldsymbol{Q}\frac{\partial \boldsymbol{H}}{\partial z}\right). \tag{21}$$

After that, carry out the inverse Fourier transformation on Equation (21) to yield

$$\frac{\partial \boldsymbol{h}}{\partial t} + \boldsymbol{P}\frac{\partial \boldsymbol{h}}{\partial x} + \boldsymbol{Q}\frac{\partial \boldsymbol{h}}{\partial z} = -2\alpha \boldsymbol{h} - \alpha^2 \int \boldsymbol{h}\mathrm{d}t - \alpha \boldsymbol{P}\frac{\partial \int \boldsymbol{h}\mathrm{d}t}{\partial x} - \alpha \boldsymbol{Q}\frac{\partial \int \boldsymbol{h}\mathrm{d}t}{\partial z}. \tag{22}$$

Hence, inserting the discrete format of Equation (22) into Equation (2) yields the required MRT-LBM expression with PML attenuation term. Note that the form of α is also a monotonic function with x or z as the independent variable. Generally speaking, the PML absorbing boundary shows a more remarkable effect than the

viscous absorbing boundary, but the value range of α has to be strictly controlled to avoid instability.

2.4. Joint absorbing boundary

In view of the fact that the viscous absorbing boundary and the PML absorbing boundary apply to the same type of absorption layer and their attenuation functions have a similar form, why not couple them together to develop a new joint absorbing boundary to achieve a better absorption effect? Theoretically, the JAB has a more effective absorption function under the premise of increasing a certain amount of calculation, while the adjustment of attenuation parameters is more flexible. Based on this, taking the right boundary as an example, the discrete format of the modified MRT-LBM scheme with JAB can be expressed as

$$\begin{aligned}\boldsymbol{f}(\boldsymbol{x}+\boldsymbol{c}_l\Delta t, t+\Delta t)-\boldsymbol{f}(\boldsymbol{x},t) = &-\Delta t\boldsymbol{M}^{-1}\boldsymbol{S}^{*}[\boldsymbol{m}(\boldsymbol{x},t)-\boldsymbol{m}^{\mathrm{eq}}(\boldsymbol{x},t)] \\ &-\alpha\Delta t\left(2\boldsymbol{h}+\alpha\boldsymbol{W}\right. \\ &+\boldsymbol{P}\frac{\boldsymbol{W}_{x,z}-\boldsymbol{W}_{x-1,z}}{\Delta x} \\ &\left.+\boldsymbol{Q}\frac{\boldsymbol{W}_{x,z}-\boldsymbol{W}_{x,z-1}}{\Delta z}\right),\end{aligned} \tag{23}$$

where the modified relaxation matrix $\boldsymbol{S}^{*}=diag(s_1,s_2^{*},s_3,s_4,s_5,s_6,s_7,s_8^{*},s_9^{*})$ and the auxiliary quantity $\boldsymbol{W}=\int\boldsymbol{h}\mathrm{d}t$. The transformation matrix $\boldsymbol{M}$ of D2Q9 is given in Appendix A.

In addition, there are two quantities, namely $\alpha(x)$ and $g(x)$, left to be discussed. The choice of these two attenuation functions has a certain influence on the absorption effect. For both, it is crucial to determine the type of attenuation function, the thickness of the absorbing layer and the attenuation constant associated with it. The strategy in this paper is to obtain the corresponding local optimum solution by means of numerous repetitive numerical experiments. This is done as follows.

Step 1: select some commonly used function types, e.g., linear, parabolic, sine, etc. By careful comparison, the polynomial functions (Chen, 2010; Modave et al., 2014) are adopted here

$$\begin{cases} g(x)=r_1\left(\dfrac{x}{L}\right)^{n_1}, \\ \alpha(x)=r_2\left(\dfrac{x}{L}\right)^{n_2}, \end{cases} \tag{24}$$

where L is the thickness of the absorbing layer, r_1 and r_2 are different attenuation constants, n_1 and n_2 are different indexes, varying from 0 to 4.

Step 2: select several sets of acceptable absorbing layer thicknesses, e.g., layers 10, 15, 20, 25, etc.
Step 3: select different magnitudes of attenuation coefficients, e.g., 10^{-5}, 10^{-3}, 10^{-1}, etc.

Once the three sets of parameters are available, normal numerical simulations can be carried out, and by comparing the absorption effects of truncated boundary reflections in different cases (i.e., by looking at the wavefield snapshots or calculating the energy of the reflected waves, which will be described later), the optimized attenuation function can be selected and obtained. This is, of course, a tedious preparatory task, but it is also necessary.

With these foundations in place, finally, Algorithm 1 briefly describes the process of seismic wavefield modeling by MRT-LBM with the JAB scheme.

Algorithm 1. Seismic wavefield modeling by MRT-LBM loaded with the joint absorbing boundary

Input: $N_x, N_z, N_t, L, \boldsymbol{w}, \boldsymbol{c}, \boldsymbol{S}, \boldsymbol{M}$.

Output: Wavefields at each time step.

Calculating the modified relaxation matrix: $\boldsymbol{S}\rightarrow\boldsymbol{S}^{*}$;

for $t=0:\Delta t:N_t\Delta t$ **do**

Calculating the equilibrium distribution function and its perturbation component:

$\rho,\boldsymbol{u}\rightarrow\boldsymbol{f}^{\mathrm{eq}}$, $\boldsymbol{f}^{\mathrm{eq}}\rightarrow\boldsymbol{h}$;

Performing collision step in moment space: $\boldsymbol{f},\boldsymbol{f}^{\mathrm{eq}},\boldsymbol{S}^{*}\rightarrow\boldsymbol{f}^{+}$;

Loading the joint absorbing boundary: $\boldsymbol{f}^{+},\boldsymbol{h}\rightarrow\boldsymbol{f}^{*}$;

Conducting steaming step in velocity space: $\boldsymbol{f}^{*}(\boldsymbol{x})\rightarrow\boldsymbol{f}(\boldsymbol{x}+\Delta\boldsymbol{x})$;

Applying boundary conditions (e.g., periodic) to assign values to distribution functions of unknown particles on the boundary;

Calculating the macroscopic quantities: $\boldsymbol{f},\boldsymbol{c}\rightarrow\rho,\boldsymbol{u}$;

end for

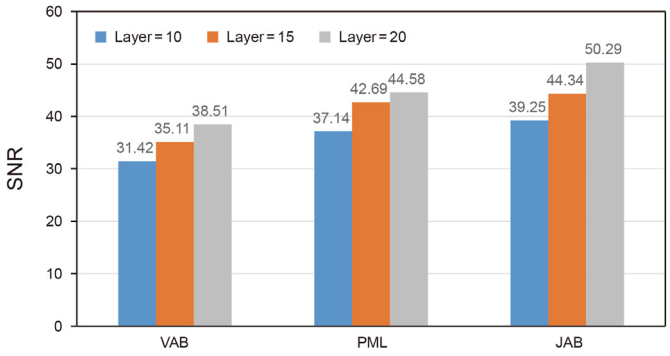

Fig. 6. The *SNR*s calculated by Equation (26) for different absorption schemes with absorption layers of 10, 15 and 20.

Table 2
The parameters of optimized attenuation functions in Equation (24).

	n_1	n_2	r_1	r_2
VAB	3	×	0.005	×
PML	×	2.5	×	0.00002
JAB	3	2.5	0.003	0.00003

3. Numerical examples

This section consists of four numerical simulation examples. First, the accuracy of wavefield simulation by MRT-LBM is tested on a homogeneous model; then the effectiveness of JAB is verified on a 2D homogeneous model, a modified 2D British petroleum (BP) gas-cloud model and a 3D homogeneous model.

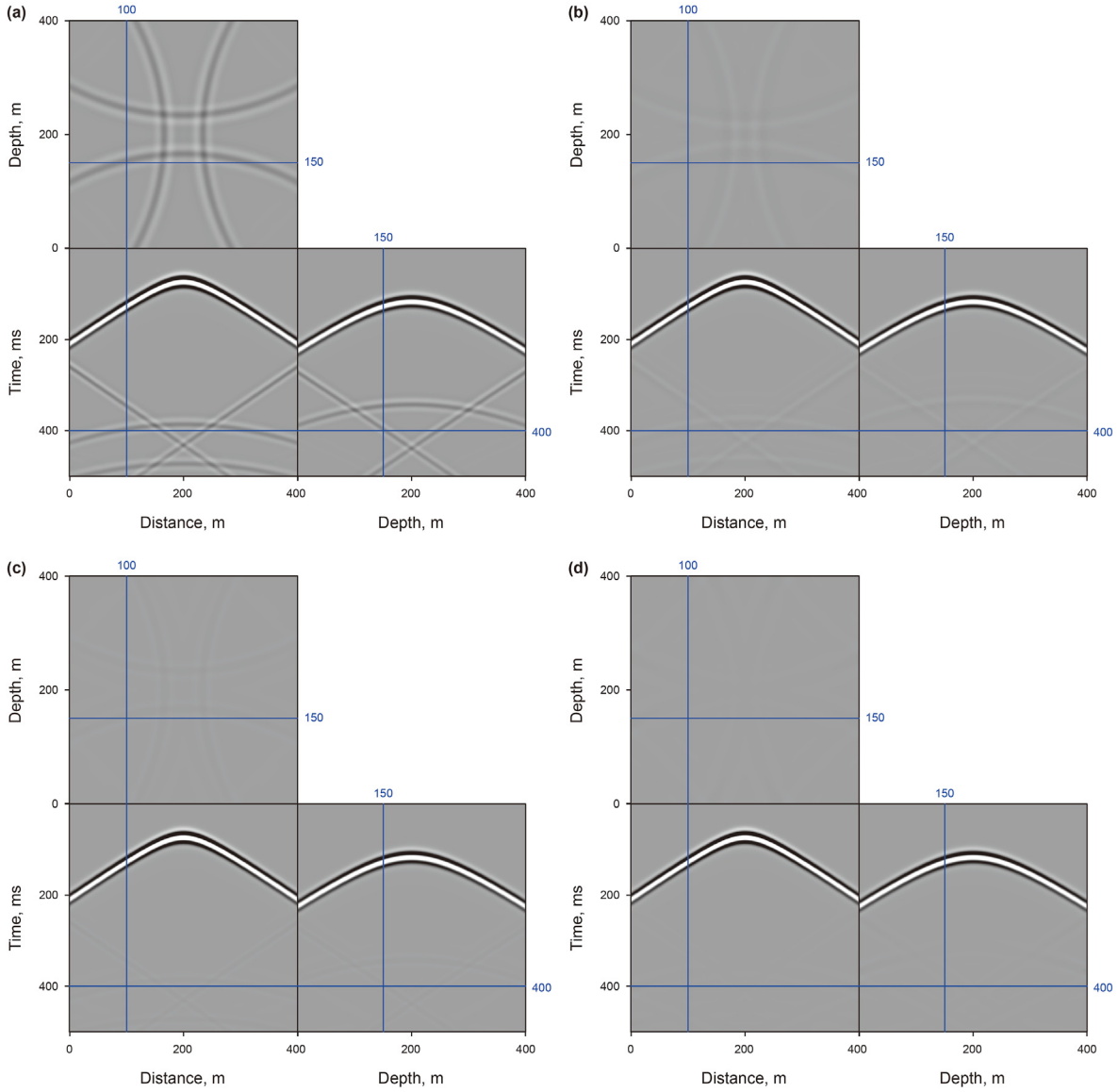

Fig. 7. For the 2D homogeneous model, wavefield snapshots at $t = 400$ ms, seismic records at $x = 100$ m and $z = 150$ m computed by MRT-LBM with (a) no absorbing boundary, (b) VAB, (c) PML, and (d) JAB schemes.

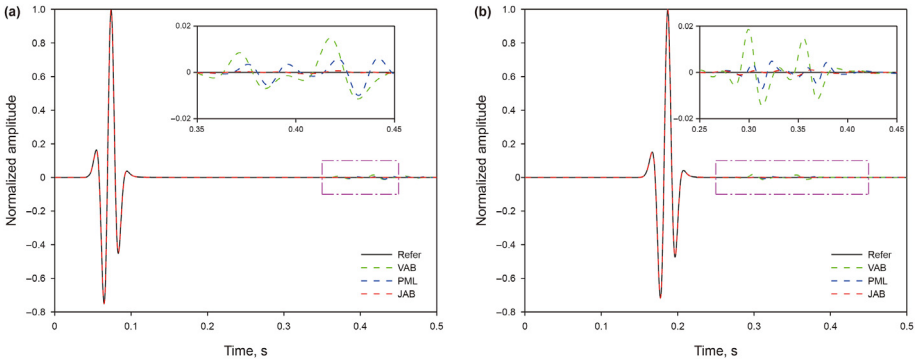

Fig. 8. Seismic records at the (a) 6th and (b) 8th receivers in the 2D homogeneous medium. The pink boxes indicate the boundary reflections are enlarged in this figure.

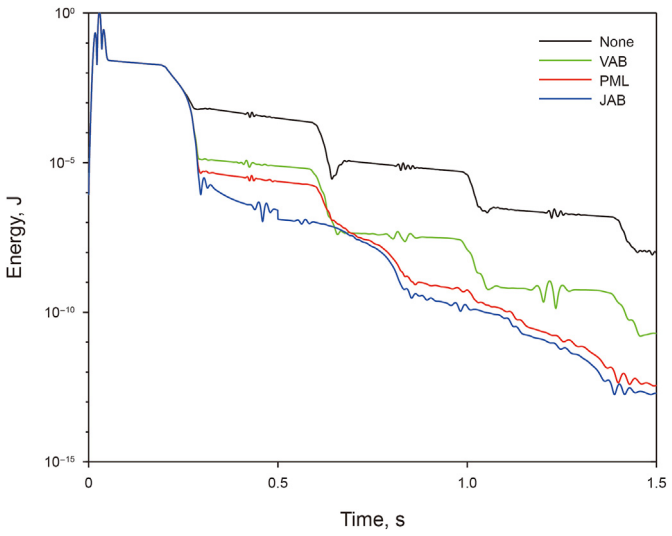

Fig. 9. The instantaneous total wavefield energy in the internal 2D homogeneous region calculated by Equation (27).

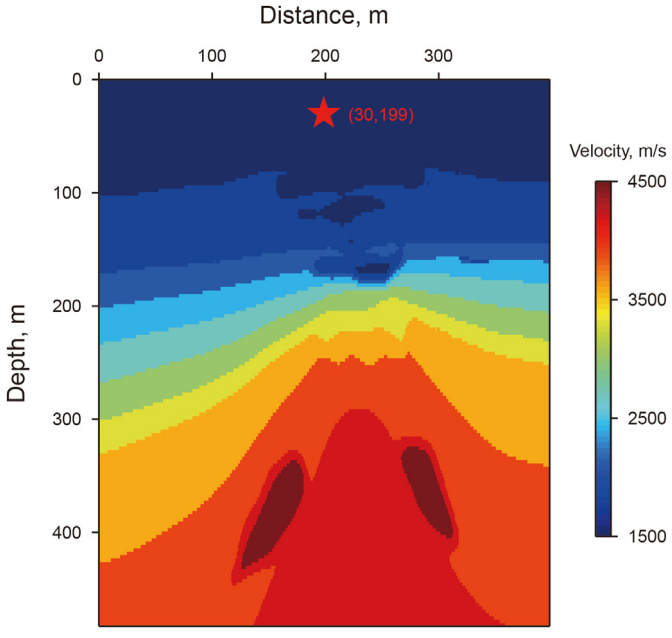

Fig. 10. The velocity of modified BP model, whose maximum and minimum velocities are 4500 m/s and 1500 m/s, respectively. The red star indicates a source.

3.1. Accuracy of MRT-LBM

The work of Xia et al. (2017) demonstrates the wavefields calculated by SRT-LBM are comparable to the corresponding finite-difference solutions of wave equation. Before loading MRT-LBM with an absorbing boundary scheme, it is necessary to discuss the accuracy of MRT-LBM performing seismic simulations. Here, for simplicity, the finite-difference method solving the wave equation is utilized as the reference scheme. We employ three schemes, namely SRT-LBM, MRT-LBM, and FDM, for the wavefield evolution on a 2D homogeneous model. Noting that the FDM here uses a much smaller temporal sampling interval to maintain high numerical accuracy, other simulation parameters are the same.

The homogeneous 2D model is 400 m in the x-direction and 400 m in the z-direction. The spatial interval in both the x- and z-direction is 1 m, and the temporal interval is 0.5 ms (For FDM, it is 0.01 ms). A Ricker wavelet source with a dominant frequency of 30 Hz is located at (200 m, 200 m). The velocity of the P-wave is 1154 m/s, and the density is 1000 kg/m^3. Fig. 3a extracts the wave profiles at the same depth, and similarly, Fig. 3b extracts the wave profiles at the same horizontal position. By visual observation, we find that the results obtained by these three schemes are almost indistinguishable. In addition, we show the vibrations recorded at four positions in Fig. 3c, from which the same conclusion as the above subplots can be acquired. Further, we compare quantitatively the differences between the seismic traces obtained with MRT-LBM and SRT-LBM concerning the reference trace calculated by the following formula

$$\eta_L = \frac{\sum_t (A_{FDM}(t) - A_L(t))^2}{\sum_t A_{FDM}^2(t)} \times 100\%, \tag{25}$$

where $A_{FDM}(t)$ stands for the seismic trace obtained by the FDM method, $L = SRT$ or MRT represents the simulated data obtained by SRT-LBM or MRT-LBM, respectively. The quantitative results are displayed in Table 1. It is seen from Table 1 that the accuracy of MRT-LBM is a little higher than that of SRT-LBM, mainly because MRT-LBM owns several free adjustable relaxation parameters, some of which affect the numerical accuracy.

3.2. JAB effect for the 2D homogeneous model

After we analyze the accuracy of the MRT-LBM simulated seismic wavefield, one may then be curious about the effects of the JAB proposed in this paper. The simplest geological model, i.e., a 2D homogeneous model with 1154 m/s velocity and 1000 kg/m^3 density, is tested here. The size of the internal area and the setup of

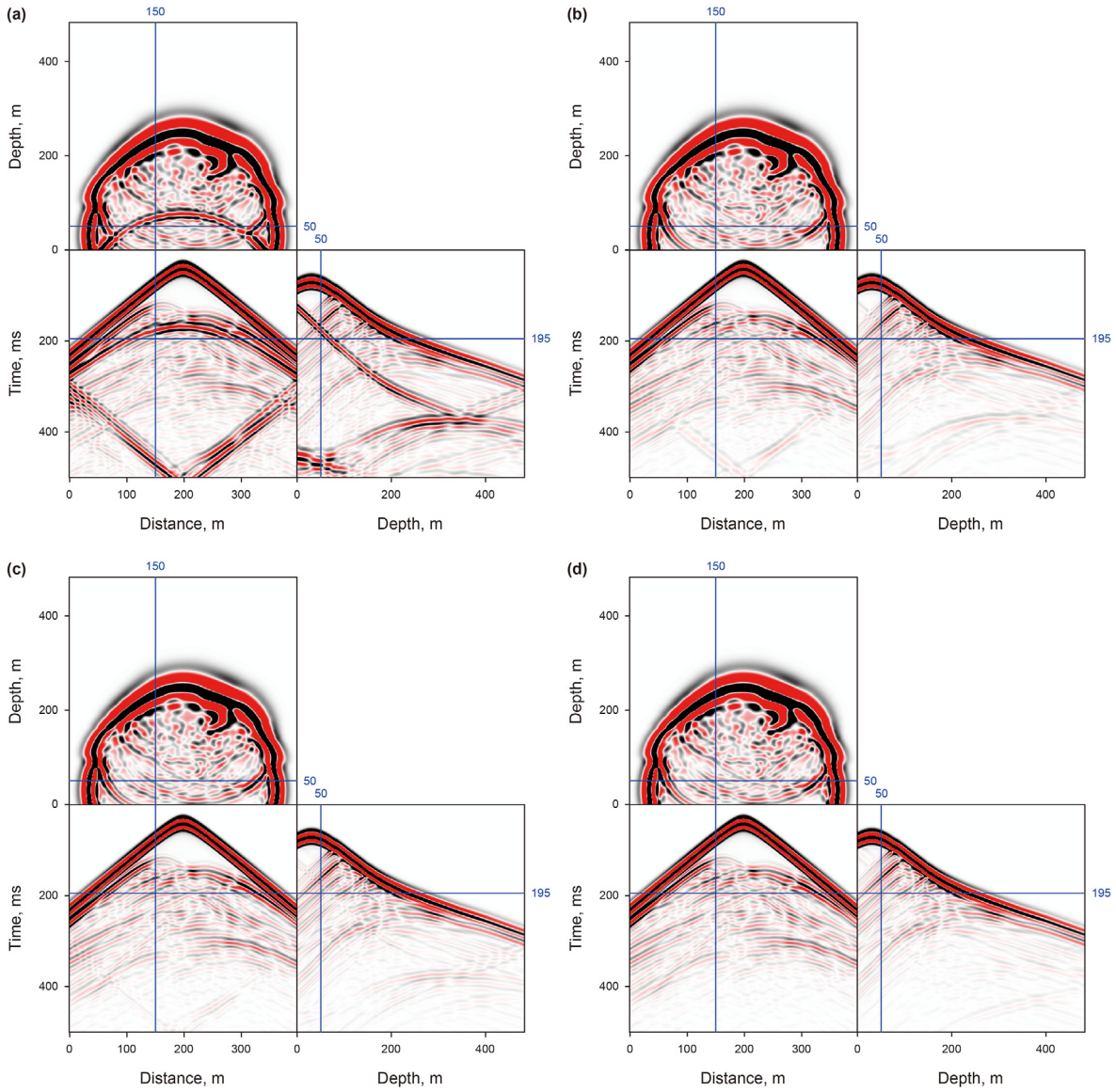

Fig. 11. Wavefields in the 2D modified BP model. In each subplot there are snapshots at $t = 195$ ms, seismograms at $x = 150$ m and $z = 50$ m computed by MRT-LBM with (a) no absorbing boundary, (b) VAB, (c) PML, and (d) JAB schemes.

the observation system are shown in Fig. 4, and the external absorption layer is in the form of four trapezoidal combinations, as shown in Fig. 5. The relaxation parameters in the internal area are $s_1 \sim s_9 = (0, 1.9, 1.7, 0, 1.8, 0, 1.8, 1.9, 1.9)$. To preliminarily compare the effectiveness of three absorbing boundary schemes, their signal-to-noise ratio (*SNR*) when the thickness of the absorbing layer is 10, 15, and 20 are calculated by the following equation

$$SNR = \frac{1}{8}\sum_{l=1}^{8} 10\lg\left(E_l^{\mathrm{dir}} \Big/ E_l^{\mathrm{ref}}\right), \tag{26}$$

where E_l^{dir} and E_l^{ref} stand for the direct wave energy and reflected wave energy of the l-th receivers in Fig. 4, respectively. Both attenuation functions used here are of Equation (24), and their corresponding attenuation coefficients, which are closely related to the thickness of the absorption layer, are optimized by certain numerical tests.

The *SNR*s calculated for the three absorbing boundaries with different absorption layers are depicted in Fig. 6, from which it can be intuitively found that, in general, the more layers the better the absorption effect; besides, for the same absorption layers, the JAB absorption effect is ranked the best and VAB the worst.

Then, wavefield snapshots and seismic records simulated using MRT-LBM combined with different absorbing boundaries in the homogeneous medium are shown in Fig. 7. The thickness of the absorption boundary is 20 layers, and other parameters of optimized attenuation functions are shown in Table 2. Fig. 7a corresponds to no absorbing boundary, and Fig. 7b, c, and 7d correspond to VAB, PML, and JAB, respectively. By comparing these four subplots, it is clear that the JAB has the best absorption effect and the corresponding truncated boundary reflection is quite weak. In addition, we show the vibration curves at the 6th and 8th receivers in Fig. 8a and b, respectively, where the pink dashed rectangles indicate the boundary reflections. To clearly view the details, the signals in the rectangles are enlarged in Fig. 8. The reference solution without boundary reflections (black line) is acquired by expanding the simulation area. Fig. 8 reveals that the JAB (the red

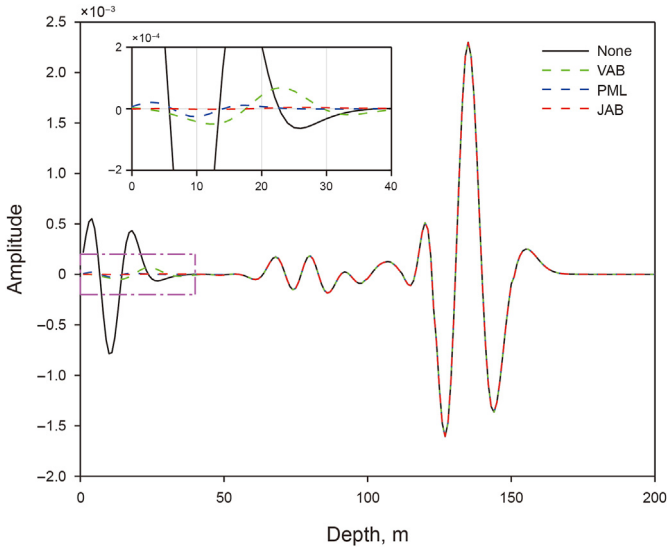

Fig. 12. Seismic wave profile at $t = 250$ ms and $x = 200$ m in the 2D modified BP model, and the zoomed-in part of the pink rectangle.

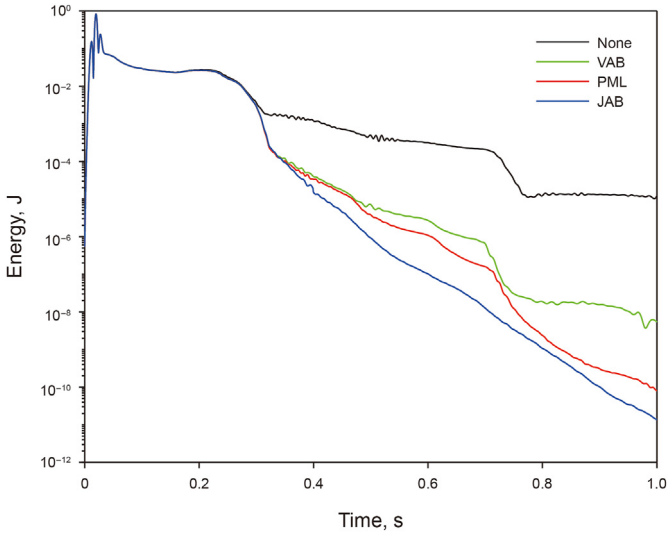

Fig. 13. The instantaneous total wavefield energy in the internal region calculated by Equation (27) in the 2D modified BP model.

dashed line) has minimal boundary reflections, which is exactly the performance one expects. Further, the energy over the entire simulation region is quantified as the wavefield moves in and out of the boundary. For simplicity, the sum of squared amplitudes at all spatial points at a given moment

$$E_{\text{total}}(t) = \sum_{j=1}^{Nx} \sum_{l=1}^{Nz} A_{j,k}^2(t), \tag{27}$$

is taken as the total wavefield energy at that moment. It should be noted that the energy of the absorption region is not included in this formula.

Fig. 9 visualizes the variation of wavefield energy with propagation time when different absorbing boundary schemes are applied. Overall, the total wavefield energy decreases with time even without the absorbing boundaries, which is partly attributed to the fact that the LBM simulates a viscous acoustic wavefield. On the other hand, the wavefield energy corresponding to JAB decays fastest and most significantly when the wave enters the absorption layer, and the energy returns into the inner region is approximately 5.5 orders lower compared to that of the direct wave.

3.3. JAB effect for the 2D modified BP model

We further validate the applicability of this joint absorbing boundary to complex models, such as the modified 2D BP model displayed in Fig. 10, where the red star indicates the location of the Ricker wavelet source. The velocity of the P-wave is shown in Fig. 10, and the density is 1000 kg/m^3. Likewise, the thickness of the absorption layers is 20, and the attenuation functions are the same as in the previous example. The spatial interval in both the x- and z-direction is 1 m, and the temporal interval is 0.5 ms. The relaxation parameters in the internal area are $s_1 \sim s_9 = (0, 1.9, 1.9, 0, 1.9, 0, 1.9, 1.9, 1.9)$. The four subplots of Fig. 11 present the wavefield snapshots and seismic records. Fig. 11a shows the wavefields derived without boundary treatment and Fig. 11b–d shows those obtained with VAB, PML, and JAB, respectively. The positions of the cyan arrows in this figure indicate the dominant truncated boundary reflections. As observed in Fig. 11a, the truncated boundary reflection energy severely interferes with the effective waves from interfaces. By comparing Fig. 11a–d, we learn that the absorption efficiency of JAB is the most significant for the same number of absorption layers.

The wave profile at $t = 250$ ms and $x = 200$ m displayed in Fig. 12 is taken for a clear comparison. The signals shallower than 50 m are reflections from the upper boundary, which is framed by the pink dashed rectangle and is zoomed in at the top-left area. It is seen that JAB has a remarkable truncated boundary absorption performance. Also, the curves of energy variation with time for the whole internal region are depicted in Fig. 13, from which we can draw a similar conclusion. This implies that the JAB scheme is also applicable to 2D complex media.

3.4. JAB effect for the 3D homogeneous model

Finally, we try to check the effectiveness of the MRT-LBM-based joint absorbing boundary in a 3D homogeneous model. For the sake of simplicity, the 3D discrete velocity model is chosen as D3Q15 introduced in Appendix A. It is not difficult to generalize the joint absorbing boundary from two dimensions to three dimensions, and the details are further described in Appendix B. The size of the internal model is $150 \times 150 \times 150$ grids. The spatial interval in both the x- and z-direction is 1 m, and the temporal interval is 0.5 ms. The location of a shot-point is $(10, 10, 10)$ in grid. The thickness of the absorption layer is 20, and the selected attenuation functions are the same as in the previous example. The relaxation parameters in the internal area are $s_1 \sim s_{15} = (0, 1.9, 1.9, 0, 1.9, 0, 1.9, 0, 1.9, 1.9, 1.9, 1.9, 1.9, 1.9, 1.9)$. Fig. 14 illustrates 3D wavefield snapshots obtained by loading different absorbing boundaries, where three slices at $x = 50$ m, $y = 50$ m, and $z = 50$ m are shown, respectively. Comparing the boundary reflections indicated by the cyan arrows in the four subplots, we find that the unfavorable reflections in Fig. 14d are pretty weak and almost indistinguishable. This example demonstrates that the JAB is also applicable to MRT-LBM-based wavefield simulations for a 3D homogeneous medium.

In addition to accounting for the differences in absorption effects, it is essential to discuss the computational efficiency of the three schemes. Theoretically, PML and JAB consume more time than VAB in terms of the complexity of algorithms. To verify this, the 3D homogeneous model with a large simulation step is used as an example. The simulations are performed on a PC configuration with a 3 GHz Intel processor and 16 GB of RAM, and with the same C programming and running environment. Table 3 exhibits the

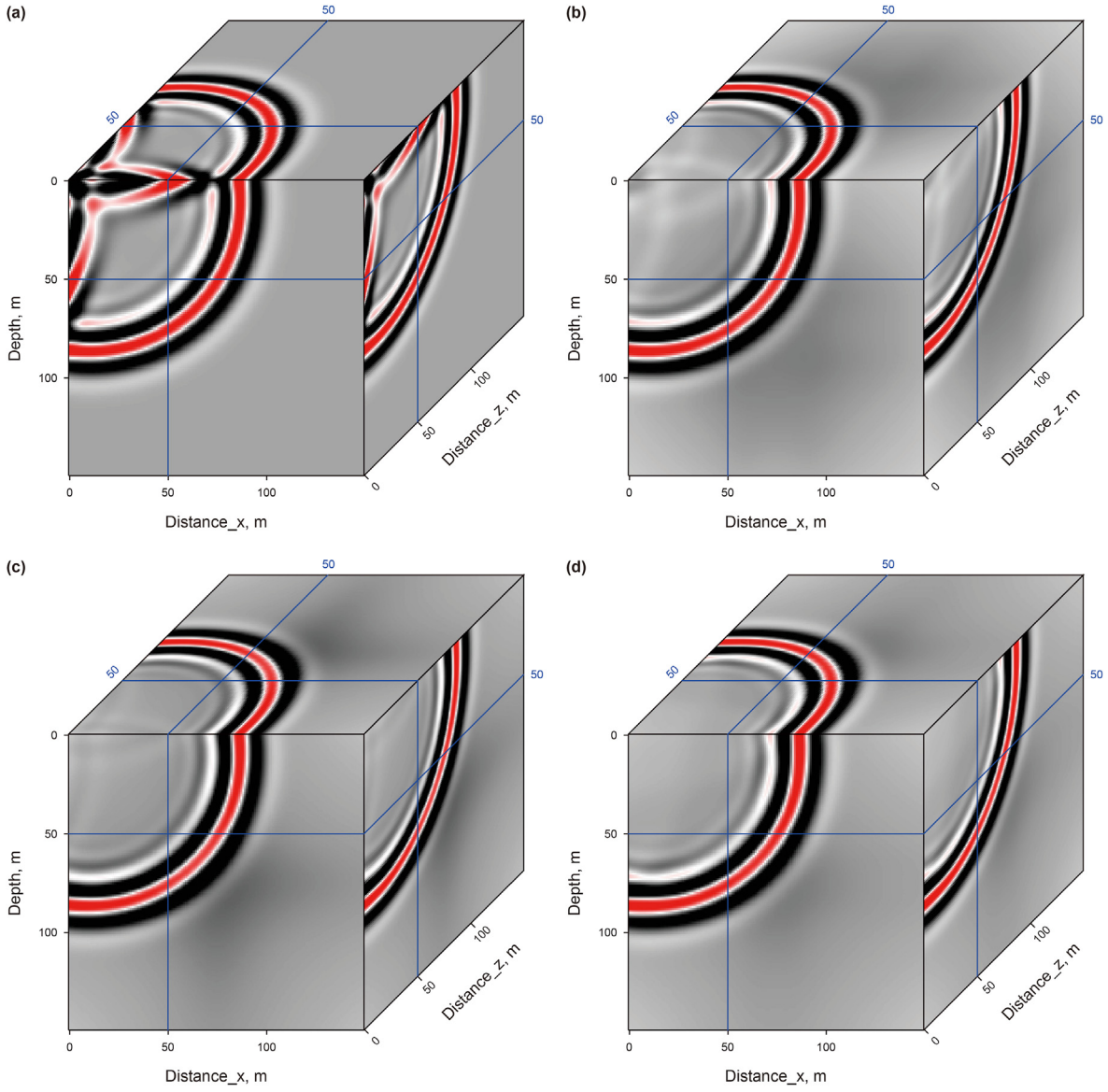

Fig. 14. Wavefields in the 3D homogeneous model. Snapshots at $x = 50$ m, $y = 50$ m, and $z = 50$ m computed by MRT-LBM with (a) no absorbing boundary, (b) VAB, (c) PML, and (d) JAB schemes.

Table 3
The elapsed time of MRT-LBM accompanied by different absorption schemes and the corresponding additional time consumption percentages calculated by Equation (28).

Scheme	None	VAB	PML	JAB
Elapsed time, s	996	1008	1085	1098
β, %	0	1.2	8.9	10.2

elapsed times and corresponding time consumption percentages β obtained by the following equation for different schemes

$$\beta = \frac{T_\alpha - T_{\text{None}}}{T_{\text{None}}} \times 100\%, \tag{28}$$

where T_{None} represents the elapsed time without absorbing boundary, T_α stands for the elapsed time with VAB, PML, or JAB. As seen from Table 3, for the same number of absorption layers, the time consumed by VAB does not differ much from the reference case. In contrast, JAB, due to the complexity of the algorithm, increases the calculation time by about 10%, while improves significantly the absorption effect. In reality, parallelism is a notable feature of LBM. Therefore, the computational efficiency of MRT-LBM can be improved by a certain parallel computing scheme (e.g., Campos et al., 2016; Takáč and Petráš, 2021), which is beyond the scope of this paper.

4. Discussion

Conventional seismic acoustic wavefield modeling is generally done by solving the macroscopic wave equations, while in this paper, we use an alternative scheme, which is MRT-LBM, that does not depend on the wave equation at the mesoscopic scale. Xia et al. (2017) verified that the wavefields simulated by SRT-LBM have a high degree of agreement with those based on the Kelvin-Voigt viscoacoustic equation. We further compare the wavefields simulated by MRT-LBM to those by SRT-LBM and find that MRT-LBM simulation is more accurate than SRT-LBM simulation, mainly

because MRT-LBM can freely adjust more relaxation parameters. Also, due to its characteristics, MRT-LBM is superior to SRT-LBM in terms of stability, numerical dispersion suppression, etc., which of course must be acknowledged as inevitably bringing a 10–20% computational burden (Krüger et al., 2017).

Most notably, we successfully extend the viscous absorbing boundary and PML absorbing boundary based on the SRT-LB equation to the MRT-LB equation, and we have further constructed a joint absorbing boundary and embedded it into the general MRT-LB equation (i.e., Equation (23) and B-1). By comparison, this scheme is the best among the three schemes in terms of absorption efficiency; however, it has the highest computational complexity and takes about 1% more computational effort than the PML absorption boundary. This joint absorbing boundary has been tested on both simple 2D and 3D media with relatively good results, which has laid the foundation for its wide application in wavefield simulations.

However, there are four points that should be noted. First, the viscous absorbing boundary can usually achieve an acceptable absorbing effect in the case of a relatively large number of absorbing layers, its algorithm is simpler and more applicable (Xu and Sagaut, 2013). Which kind of absorption scheme is needed depends on the specific situation. Second, both the VAB and the PML need reasonable coefficients of their attenuation functions, otherwise, instability may occur. Therefore, for JAB, as a combination of VAB and PML, one should pay more attention to the two attenuation coefficients. Third, for JAB in this paper, the attenuation functions are all of the polynomial type, and the two constant coefficients are optimized by numerical experiments. However, this process is troublesome and lacks theoretical formulas to guide it. How to adjust the attenuation coefficients adaptively is a direction worthy of future research. Finally, for the JAB scheme as well as MRT-LBM itself, the problem of large computation should be addressed in the future, such as trying some parallel computing schemes (Takáč and Petráš, 2021).

5. Conclusions

We use MRT-LBM as a new scheme for modeling seismic acoustic wavefields in the field of exploration seismology and verify that MRT-LBM is more accurate than SRT-LBM in terms of waveforms. In addition, to better solve the severe truncated boundary reflection problem encountered by MRT-LBM in simulating wavefields, we analogize the viscous absorbing boundary and the PML absorbing boundary targeting the SRT-LB equation to the MRT-LB equation, and further, propose a joint absorbing boundary through certain combinations of these two absorbing schemes. The joint scheme is proved to have a remarkable absorption performance by numerical experiments on a 2D homogeneous model, a 2D modified BP model, and a 3D homogeneous model. The effectiveness of the joint absorbing boundary promotes MRT-LBM for modeling seismic acoustic wavefields, although its computational efficiency is slightly lower than that of the PML scheme. In a word, considering the advantages of flexible boundary strategies and complete discrete characteristics of LBM, the proposed JAB scheme for MRT-LBM will have better prospects in some media, such as complex pore structures, thanks to its high accuracy and good stability.

Declaration of competing interest

The authors declare that they have no known competing financial interests or personal relationships that could have appeared to influence the work reported in this paper. The authors acknowledge there are no conflicts of interest recorded.

Acknowledgment

This work is supported in part by the National Natural Science Foundation of China (U19B6003-04-01, 42204132, 41874130), R&D Department of CNPC (2022DQ0604-01), and China Postdoctoral Science Foundation (2020M680667, 2021T140661).

Appendix A. Transformation matrix for D2Q9 and D3Q15

The transformation matrix corresponding to D2Q9 is

$$\boldsymbol{M}=\begin{bmatrix} 1 & 1 & 1 & 1 & 1 & 1 & 1 & 1 & 1 \\ -4 & -1 & -1 & -1 & -1 & 2 & 2 & 2 & 2 \\ 4 & -2 & -2 & -2 & -2 & 1 & 1 & 1 & 1 \\ 0 & 1 & 0 & -1 & 0 & 1 & -1 & -1 & 1 \\ 0 & -2 & 0 & 2 & 0 & 1 & -1 & -1 & 1 \\ 0 & 0 & 1 & 0 & -1 & 1 & 1 & -1 & -1 \\ 0 & 0 & -2 & 0 & 2 & 1 & 1 & -1 & -1 \\ 0 & 1 & -1 & 1 & -1 & 0 & 0 & 0 & 0 \\ 0 & 0 & 0 & 0 & 0 & 1 & -1 & 1 & -1 \end{bmatrix}, \tag{A-1}$$

and that of D3Q15 is

$$\boldsymbol{M}=\begin{bmatrix} 1 & 1 & 1 & 1 & 1 & 1 & 1 & 1 & 1 & 1 & 1 & 1 & 1 & 1 & 1 \\ -2 & -1 & -1 & -1 & -1 & -1 & -1 & 1 & 1 & 1 & 1 & 1 & 1 & 1 & 1 \\ 16 & -4 & -4 & -4 & -4 & -4 & -4 & 1 & 1 & 1 & 1 & 1 & 1 & 1 & 1 \\ 0 & 1 & -1 & 0 & 0 & 0 & 0 & 1 & -1 & 1 & -1 & 1 & -1 & -1 & 1 \\ 0 & -4 & 4 & 0 & 0 & 0 & 0 & 1 & -1 & 1 & -1 & 1 & -1 & -1 & 1 \\ 0 & 0 & 0 & 1 & -1 & 0 & 0 & 1 & -1 & 1 & -1 & -1 & 1 & 1 & -1 \\ 0 & 0 & 0 & -4 & 4 & 0 & 0 & 1 & -1 & 1 & -1 & -1 & 1 & 1 & -1 \\ 0 & 0 & 0 & 0 & 0 & 1 & -1 & 1 & -1 & -1 & 1 & 1 & -1 & 1 & -1 \\ 0 & 0 & 0 & 0 & 0 & -4 & 4 & 1 & -1 & -1 & 1 & 1 & -1 & 1 & -1 \\ 0 & 2 & 2 & -1 & -1 & -1 & -1 & 0 & 0 & 0 & 0 & 0 & 0 & 0 & 0 \\ 0 & 0 & 0 & 1 & 1 & -1 & -1 & 0 & 0 & 0 & 0 & 0 & 0 & 0 & 0 \\ 0 & 0 & 0 & 0 & 0 & 0 & 0 & 1 & 1 & 1 & 1 & -1 & -1 & -1 & -1 \\ 0 & 0 & 0 & 0 & 0 & 0 & 0 & 1 & 1 & -1 & -1 & -1 & -1 & 1 & 1 \\ 0 & 0 & 0 & 0 & 0 & 0 & 0 & 1 & 1 & -1 & -1 & 1 & 1 & -1 & -1 \\ 0 & 0 & 0 & 0 & 0 & 0 & 0 & 1 & -1 & -1 & 1 & -1 & 1 & -1 & 1 \end{bmatrix}. \tag{A-2}$$

The inverse matrices of these two transformation matrices can also be determined by a simple calculation.

Appendix B. The expression of JAB for D3Q15-MRT-LBM

The discrete format of the modified MRT-LB expression based on the D3Q15 discrete velocity model accompanied by the joint absorbing boundary is represented as follows (taking the right-hand side boundary as an example)

where the modified relaxation matrix

$$\boldsymbol{f}(\boldsymbol{x}+\boldsymbol{c}_l\Delta t, t+\Delta t)-\boldsymbol{f}(\boldsymbol{x},t)=-\Delta t\boldsymbol{M}^{-1}\boldsymbol{S}^{*}[\boldsymbol{m}(\boldsymbol{x},t)-\boldsymbol{m}^{eq}(\boldsymbol{x},t)] -\alpha\Delta t\left(\begin{array}{l} 3\boldsymbol{h}+3\alpha\boldsymbol{J}+2\boldsymbol{P}\dfrac{\boldsymbol{J}_{x,y,z}-\boldsymbol{J}_{x-1,y,z}}{\Delta x}+2\boldsymbol{R}\dfrac{\boldsymbol{J}_{x,y,z}-\boldsymbol{J}_{x,y-1,z}}{\Delta y}+2\boldsymbol{Q}\dfrac{\boldsymbol{J}_{x,y,z}-\boldsymbol{J}_{x,y,z-1}}{\Delta z} \\ +\alpha^2\boldsymbol{K}+\alpha\boldsymbol{P}\dfrac{\boldsymbol{K}_{x,y,z}-\boldsymbol{K}_{x-1,y,z}}{\Delta x}+\alpha\boldsymbol{R}\dfrac{\boldsymbol{K}_{x,y,z}-\boldsymbol{K}_{x,y-1,z}}{\Delta y}+\alpha\boldsymbol{Q}\dfrac{\boldsymbol{K}_{x,y,z}-\boldsymbol{K}_{x,y,z-1}}{\Delta z} \end{array}\right), \tag{B-1}$$

$$\boldsymbol{S}^{*}=diag\left(s_1,s_2^{*},s_3,s_4,s_5,s_6,s_7,s_8,s_9,s_{10}^{*},s_{11}^{*},s_{12}^{*},s_{13}^{*},s_{14}^{*},s_{15}\right), \tag{B-2}$$

$$s_l^{*}(x)=\frac{1}{1/s_l+g(x)},\quad l=2,10,11,\cdots,14, \tag{B-3}$$

and the two auxiliary quantities $\boldsymbol{J},\boldsymbol{K}$.

$$\boldsymbol{J}=\int\boldsymbol{h}\mathrm{d}t,\quad \boldsymbol{K}=\int\boldsymbol{J}\mathrm{d}t, \tag{B-4}$$

and the three diagonal matrices $\boldsymbol{P},\boldsymbol{Q},\boldsymbol{R}$.

$$\boldsymbol{P}=diag(c_{xl}),\boldsymbol{Q}=diag(c_{zl}),\boldsymbol{R}=diag\left(c_{yl}\right),l=1,2,\cdots 15. \tag{B-5}$$

In addition, the discrete velocity sets and weighting factors corresponding to D3Q15 are shown in Equations (5) and (7) described earlier, respectively.

References

Aslan, E., Taymaz, I., Benim, A.C., 2014. Investigation of the lattice Boltzmann SRT and MRT stability for lid driven cavity flow. Int. J. Mater., Mech. Manuf. 2 (4), 317–324. https://doi.org/10.7763/ijmmm.2014.v2.149.

Ba, J., Nie, J.X., Cao, H., Yang, H.Z., 2008. Mesoscopic fluid flow simulation in double-porosity rocks. Geophys. Res. Lett. 35 (4), L04303. https://doi.org/10.1029/2007gl032429.

Berenger, J.P., 1994. A perfectly matched layer for the absorption of electromagnetic waves. J. Comput. Phys. 114 (2), 185–200. https://doi.org/10.1006/jcph.1994.1159.

Campos, J.O., Oliveira, R.S., dos Santos, R.W., Rocha, B.M., 2016. Lattice Boltzmann method for parallel simulations of cardiac electrophysiology using GPUs. J. Comput. Appl. Math. 295, 70–82. https://doi.org/10.1016/j.cam.2015.02.008.

Chai, Z., Shi, B., 2020. Multiple-relaxation-time lattice Boltzmann method for the Navier-Stokes and nonlinear convection-diffusion equations: modeling, analysis, and elements. Phys. Rev. E 102 (5), 023306. https://doi.org/10.1103/physreve.102.023306.

Chai, Z., Zhao, T.S., 2012. Effect of the forcing term in the multiple-relaxation-time lattice Boltzmann equation on the shear stress or the strain rate tensor. Phys. Rev. E 86 (1), 016705. https://doi.org/10.1103/physreve.86.016705.

Chen, H., Zhou, H., Li, Y., 2014. Application of unsplit convolutional perfectly matched layer for scalar arbitrarily wide-angle wave equation. Geophysics 79 (6), T313–T321. https://doi.org/10.1190/geo2014-0103.1.

Chen, K.Y., 2010. Study on perfectly matched layer absorbing boundary condition. Geophys. Prospect. Pet. 49 (5), 472–477. https://doi.org/10.3969/j.issn.1000-1441.2010.05.006.

Chen, S., Doolen, G.D., 1998. Lattice Boltzmann method for fluid flows. Annu. Rev. Fluid Mech. 30 (1), 329–364. https://doi.org/10.1146/annurev.fluid.30.1.329.

d'Humières, D., 1992. Generalized lattice Boltzmann equations, in rarefied gas dynamics: theory and simulations. In: Shizgal, B.D., Weaver, D.P. (Eds.), Prog. Aeronaut. Astronaut., vol. 159, pp. 450–458. https://doi.org/10.2514/4.866319.

d'Humières, D., 2002. Multiple–relaxation–time lattice Boltzmann models in three dimensions. Philos. Trans. R. Soc. London, Ser. A: Math. Phys. Eng. Sci. 360 (1792), 437–451. https://doi.org/10.1098/rsta.2001.0955.

Dhuri, D.B., Hanasoge, S.M., Perlekar, P., Robertsson, J.O., 2017. Numerical analysis of the lattice Boltzmann method for simulation of linear acoustic waves. Phys. Rev. E 95 (4), 043306. https://doi.org/10.1103/physreve.95.043306.

Escande, M., Kolluru, P.K., Cléon, L.M., Sagaut, P., 2020. Lattice Boltzmann Method for wave propagation in elastic solids with a regular lattice: theoretical analysis and validation. ArXiv Prepr. ArXiv:2009.06404. https://doi.org/10.13140/RG.2.2.11264. 46084.

Feng, Y., Guo, S., Jacob, J., Sagaut, P., 2019. Solid wall and open boundary conditions in hybrid recursive regularized lattice Boltzmann method for compressible flows. Phys. Fluids 31 (12), 126103. https://doi.org/10.1063/1.5129138.

Frisch, U., Hasslacher, B., Pomeau, Y., 1986. Lattice-gas automata for the Navier-Stokes equation. Phys. Rev. Lett. 56 (14), 1505. https://doi.org/10.1103/physrevlett.56.1505.

Guo, Z., Zheng, C., Shi, B., 2002. An extrapolation method for boundary conditions in lattice Boltzmann method. Phys. Fluids 14 (6), 2007–2010. https://doi.org/10.1063/1.1471914.

Hauser, A., Verhey, J.L., 2019. Comparison of the lattice-Boltzmann model with the finite-difference time-domain method for electrodynamics. Phys. Rev. E 99 (3), 033301. https://doi.org/10.1103/physreve.99.033301.

He, X., Doolen, G.D., 2002. Thermodynamic foundations of kinetic theory and lattice Boltzmann models for multiphase flows. J. Stat. Phys. 107 (1), 309–328. https://doi.org/10.1023/A:1014527108336.

He, X., Luo, L.S., 1997. Theory of the lattice Boltzmann method: from the Boltzmann equation to the lattice Boltzmann equation. Phys. Rev. E 56 (6), 6811. https://doi.org/10.1103/physreve.56.6811.

Heubes, D., Bartel, A., Ehrhardt, M., 2014. Characteristic boundary conditions in the lattice Boltzmann method for fluid and gas dynamics. J. Comput. Appl. Math. 262, 51–61. https://doi.org/10.1016/j.cam.2013.09.019.

Jiang, C., Zhou, H., Xia, M., Tang, J., Jiang, S., Zhang, M., 2022. Stability conditions of multiple-relaxation-time lattice Boltzmann model for seismic wavefield modeling. J. Appl. Geophys. 204, 104742. https://doi.org/10.1016/j.jappgeo.2022.104742.

Jiang, C., Zhou, H., Xia, M., Tang, J., Zhang, M., An, Y., 2020. Study on absorbing boundary conditions of viscous sponge layers based on lattice Boltzmann method. EAGE Tech. Prog. Expanded Abstracts 2020 (1), 1–5. https://doi.org/10.3997/2214-4609.202010644.

Kam, E.W., So, R.M.C., Leung, R.C.K., 2007. Lattice Boltzmann method simulation of aeroacoustics and nonreflecting boundary conditions. AIAA J. 45 (7), 1703–1712. https://doi.org/10.2514/1.27632.

Klin, P., Priolo, E., Seriani, G., 2010. Numerical simulation of seismic wave propagation in realistic 3-D geo-models with a Fourier pseudo-spectral method. Geophys. J. Int. 183 (2), 905–922. https://doi.org/10.1111/j.1365-246x.2010.04763.x.

Kosloff, D.D., Baysal, E., 1982. Forward modeling by a Fourier method. Geophysics 47 (10), 1402–1412. https://doi.org/10.1190/1.1441288.

Krüger, T., Kusumaatmaja, H., Kuzmin, A., Shardt, O., Silva, G., Viggen, E.M., 2017. The lattice Boltzmann method. Springer Int. Publ. 10 (978–3), 4–15. https://doi.org/10.1007/978-3-319-44649-3_3.

Lallemand, P., Luo, L.S., 2000. Theory of the lattice Boltzmann method: dispersion, dissipation, isotropy, Galilean invariance, and stability. Phys. Rev. E 61 (6), 6546. https://doi.org/10.1103/physreve.61.6546.

Latt, J., Chopard, B., Malaspinas, O., Deville, M., Michler, A., 2008. Straight velocity boundaries in the lattice Boltzmann method. Phys. Rev. E 77 (5), 056703. https://doi.org/10.1103/physreve.77.056703.

Marfurt, K.J., 1984. Accuracy of finite-difference and finite-element modeling of the scalar and elastic wave equations. Geophysics 49 (5), 533–549. https://doi.org/10.1190/1.1441689.

McNamara, G.R., Zanetti, G., 1988. Use of the Boltzmann equation to simulate lattice-gas automata. Phys. Rev. Lett. 61 (20), 2332. https://doi.org/10.1103/physrevlett.61. 2332.

Modave, A., Delhez, E., Geuzaine, C., 2014. Optimizing perfectly matched layers in discrete contexts. Int. J. Numer. Methods Eng. 99 (6), 410–437. https://doi.org/10.1002/nme.4690.

Mohammed, S., Reis, T., 2021. Lattice Boltzmann method with moment-based boundary conditions for rarefied flow in the slip regime. Phys. Rev. E 104 (4), 045309. https://doi.org/10.1103/physreve.104.045309.

Najafi-Yazdi, A., Mongeau, L., 2012. An absorbing boundary condition for the lattice Boltzmann method based on the perfectly matched layer. Comput. Fluids 68, 203–218. https://doi.org/10.1016/j.compfluid.2012.07.017.

O'Brien, G.S., Nissen-Meyer, T., Bean, C.J., 2012. A lattice Boltzmann method for elastic wave propagation in a Poisson solid. Bull. Seismol. Soc. Am. 102 (3), 1224–1234. https://doi.org/10.1785/0120110191.

Qian, Y.H., d'Humières, D., Lallemand, P., 1992. Lattice BGK models for Navier-Stokes equation. Europhys. Lett. 17 (6), 479. https://doi.org/10.1209/0295-5075/17/6/001.

Schlaffer, M.B., 2013. Non-reflecting Boundary Conditions for the Lattice Boltzmann Method. Doct. Diss.. Tech. Univ. Munich https://mediatum.ub.tum.de/?id=1129700.

Sotelo, E., Favino, M., Gibson Jr., R.L., 2021. Application of the generalized finite-element method to the acoustic wave simulation in exploration seismology. Geophysics 86 (1), T61–T74. https://doi.org/10.1190/geo2020-0324.1.
Takáč, M., Petráš, I., 2021. Cross-Platform GPU-Based implementation of lattice Boltzmann method solver using ArrayFire library. Mathematics 9 (15), 1793. https://doi.org/10.3390/math9151793.
Tang, J., Zhou, H., Jiang, C., Xia, M., Chen, H., Zheng, J., 2021. A perfectly matched layer technique applied to lattice Spring model in seismic wavefield forward modeling for Poisson's solids. Bull. Seismol. Soc. Am. 112 (2), 608–621. https://doi.org/10.1785/0120210166.
Tekitek, M.M., Bouzidi, M., Dubois, F., Lallemand, P., 2009. Towards perfectly matching layers for lattice Boltzmann equation. Comput. Math. Appl. 58 (5), 903–913. https://doi.org/10.1016/j.camwa.2009.02.013.
Vergnault, E., Malaspinas, O., Sagaut, P., 2012. A lattice Boltzmann method for nonlinear disturbances around an arbitrary base flow. J. Comput. Phys. 231 (24), 8070–8082. https://doi.org/10.1016/j.jcp.2012.07.021.
Vergnault, E., Malaspinas, O., Sagaut, P., 2013. Noise source identification with the lattice Boltzmann method. J. Acoust. Soc. Am. 133 (3), 1293–1305. https://doi.org/10.1121/1.4776181.
Viggen, E.M., 2014. The Lattice Boltzmann Method: Fundamentals and Acoustics. Ph.D. Thesis. Norw. Univ. Sci. Technol., pp. 108–178. https://www.researchgate.net/publication/263714289_The_lattice_Boltzmann_method_Fundamentals_and_acoustics
Wang, E., Ba, J., Carcione, J.M., Liu, Y., Dong, H., 2020. Effect of local fluid flow on the reflection and transmission of elastic waves at an interface between an elastic solid and a double-porosity medium. Geophysics 85 (4), T237–T256. https://doi.org/10.1190/geo2019-0294.1.
Wang, E., Carcione, J.M., Ba, J., 2019. Wave simulation in double-porosity media based on the Biot-Rayleigh theory. Geophysics 84 (4), WA11–WA21. https://doi.org/10.1190/geo2018-0575.1.
Wang, E., Carcione, J.M., Ba, J., Alajmi, M., Qadrouh, A.N., 2019. Nearly perfectly matched layer absorber for viscoelastic wave equations. Geophysics 84 (5), T335–T345. https://doi.org/10.1190/geo2018-0732.1.
Wang, H., Yuan, X., Liang, H., Chai, Z., Shi, B., 2019. A brief review of the phase-field-based lattice Boltzmann method for multiphase flows. Capillarity 2 (3), 33–52. https://doi.org/10.26804/capi.2019.03.01.
Wang, L., 2020. Enhanced multi-relaxation-time lattice Boltzmann model by entropic stabilizers. Phys. Rev. E 102 (2), 023307. https://doi.org/10.1103/physreve.102. 023307.
Xia, M., Wang, S., Zhou, H., Shan, X., Chen, H., Li, Q., Zhang, Q., 2017. Modelling viscoacoustic wave propagation with the lattice Boltzmann method. Sci. Rep. 7 (1), 1–9. https://doi.org/10.1038/s41598-017-10833-w.
Xia, M., Zhou, H., Jiang, C., Tang, J., Wang, C., Yang, C., 2022. Viscoacoustic wave simulation with the lattice Boltzmann method. Geophysics 87 (6), 1–57. https://doi.org/10.1190/geo2021-0663.1.
Xu, H., Malaspinas, O., Sagaut, P., 2012. Sensitivity analysis and determination of free relaxation parameters for the weakly-compressible MRT–LBM schemes. J. Comput. Phys. 231 (21), 7335–7367. https://doi.org/10.1016/j.jcp.2012.07.005.
Xu, H., Sagaut, P., 2013. Analysis of the absorbing layers for the weakly-compressible lattice Boltzmann methods. Comput. Phys. 245, 14–42. https://doi.org/10.1016/j.jcp.2013.02.051.
Yu, Z., Fan, L.S., 2010. Multirelaxation-time interaction-potential-based lattice Boltzmann model for two-phase flow. Phys. Rev. E 82 (4), 046708. https://doi.org/10.1103/physreve.82.046708.
Zadehgol, A., 2022. Introducing a lattice Boltzman time-domain method: a thermodynamics-based approach for simulating quantum effects. Phys. Rev. E 105 (1), 015307. https://doi.org/10.1103/physreve.105.015307.
Zang, N., Zhang, W., Chen, X., 2021. An overset-grid finite-difference algorithm to simulating elastic wave propagation in media with complex free surface topography. Geophysics 86 (4), T277–T292. https://doi.org/10.1190/geo2020-0915.1.
Zhang, J., Yan, G., Shi, X., 2009. Lattice Boltzmann model for wave propagation. Phys. Rev. E 80 (2), 026706. https://doi.org/10.1103/physreve.80.026706.
Zhuo, C., Sagaut, P., 2017. Acoustic multipole sources for the regularized lattice Boltzmann method: comparison with multiple-relaxation-time models in the inviscid limit. Phys. Rev. E 95 (6), 063301. https://doi.org/10.1103/physreve.95.063301.